Integrated Navigation using
MEMS-based Inertial, GPS and Sun Vector Measurements aboard the Spin-Stabilized PMWE-1 Sounding Rocket

Benjamin Braun*, Jochen Barf**, Markus Markgraf***

German Aerospace Center (DLR), Space Operations and Astronaut Training
Münchener Str. 20, D–82234 Weßling, Germany

* benjamin.braun@dlr.de
** jochen.barf@dlr.de
*** markus.markgraf@dlr.de

Abstract

The paper presents the design of an integrated navigation system for spin-stabilized sounding rockets that fuses angular rate and acceleration measurements of a strap-down microelectromechanical inertial measurement unit, pseudorange and range rate measurements of a GPS receiver and Sun direction vector measurements which are extracted from high-resolution high-rate video images of a camera. Its performance with respect to the position and orientation accuracy is demonstrated by means of measurements that were recorded on the PMWE-1 sounding rocket in April 2018.

1. Motivation

Range safety for sounding rockets or micro launch vehicles requires continuous and accurate position and velocity information along the flight trajectory. GPS and recently multi-constellation global navigation satellite system (GNSS) receivers have evolved as reliable tracking sensors for sounding rockets in the last two decades.

However, short signal outages of up to ten seconds and thus missing navigation fixes regularly occur, for example, due to high jerk particularly at lift-off and motor burnout or due to antenna shading at fairing jettison. In order to provide accurate position even during these outages and thus to increase the continuity of the safety-critical tracking sensor, it is proposed to augment the GNSS receiver by a microelectromechanical (MEMS) inertial measurement unit (IMU), which provides at least an inertial navigation solution during outages. IMU sensor errors are estimated in periods with available GNSS measurements as by a conventional GNSS-aided integrated navigation system. As a byproduct, the system outputs an estimate of the orientation of the sounding rocket.

Sounding rockets are generally spun up about the longitudinal axis to roll rates of up to 2,000 deg/s in the propelled ascent phase to reduce deviations of the actual trajectory from the nominally planned trajectory. Due to asymmetries of the thrust nozzle and asymmetric combustion of the propellant, the thrust force may not be perfectly aligned with the longitudinal axis but may have a small lateral component. By means of the spinning, this lateral force does not act in one certain direction but largely cancels itself over one revolution such that the lateral net force virtually vanishes. Depending on the mission, the rocket is de-spun after burnout of the motor(s) by a yo-yo de-spin system.

The high rotation rate about the longitudinal axis together with the high acceleration during the propelled phase cause large linear and g-dependent scale factor errors on the gyroscope measurements. Consequently, the orientation error about the longitudinal axis grows fast, may subsequently transform to the two lateral axes if motions are mechanically coupled or the rocket is actively reoriented, and finally degrades the inertial position and velocity solution in case of outages. Furthermore, the measurement range of the roll axis gyroscope has to cover the maximum expected spin rate, which limits the measurement resolution.

For this reason, dedicated roll-isolated inertial navigation platforms were developed in the second half of the last century for spinning flight vehicles [1]. The IMU is mounted on a gimbal that can freely rotate about the longitudinal axis. By means of a torque motor, a revolution counter and a controller, the spin rate is compensated such that the IMU and particularly the roll axis gyroscope merely experience a remaining roll rate that stems from the inertia of the gimbal and the dynamics of the control loop controlling the rotational speed of the gimbal. One example for such

Benjamin Braun, Jochen Barf, Markus Markgraf

a high precision navigation instrument is Inertial Science's DMARS-R platform [2], which is regularly applied on DLR MORABA's sounding rockets. Since these roll-isolated inertial navigation platforms are only provided by very few manufactures, are subject to International Traffic in Arms Regulations (ITAR), are damageable by high mechanical loads caused by high acceleration and jerk and are expensive, it is sought for alternatives that use commercial off-the-shelf strapdown IMU instead but provide comparable navigation performance.

The addressed disadvantages of strapdown IMU have, therefore, to be encountered by the use of additional aiding sensors that particularly restrict the growth of the orientation error with time. The IMU and aiding measurements are fused by an integrated navigation filter. Besides GNSS receivers that provide position and velocity aiding measurements, Sun sensors, Earth horizon sensors, magnetic field sensors or star tracker are possible candidates for orientation aiding. However, the fusion of the different sensor measurements comes along with increased system complexity and algorithmic effort. In order to obtain the system robustness of a self-contained, roll-isolated and purely inertial navigation platform, effective means of fault detection and isolation have to be implemented and applied to the measurements of the single sensors.

There is a special interest in using MEMS inertial sensors because of their small size, mechanical robustness and low costs. In the last decade, the grade of MEMS inertial sensors has much improved and sensors of tactical grade have come into the market. However, MEMS-based sensors are even more challenging on spin-stabilized sounding rocket applications since these sensors make use of Coriolis forces that act on a vibrating proof mass and are, therefore, prone to measurement errors because of high accelerations. This is especially a problem during the propelled flight phase when the rocket is accelerated in longitudinal direction with up to 30 g.

This paper presents a feasibility study of an integrated navigation system on a spin-stabilized sounding rocket, PMWE-1, that fuses acceleration and angular rate measurements of a MEMS IMU, pseudorange and range rate measurements of a GPS receiver and Sun direction vector measurements that are extracted from video images of a camera. PMWE-1 was a single-stage sounding rocket and was launched in April 2018 by DLR MORABA. Aboard of PMWE-1, there were a Sensonor STIM300 MEMS IMU, a DLR Phoenix GPS receiver and the low-cost action camera GoPro HERO3+. The camera was originally intended to watch the deployment and unfolding of the drogue and main parachutes, but it turned out that the captured images could also be used for navigation purposes because the Sun is well visible in the images. The image processing algorithm was originally developed to detect Earth horizon ellipses and hyperbolae, and with minor adaptions, it was enabled to capture the midpoint of the Sun in the images. For the feasibility study, all data were processed post-flight. One important issue, for example, is the time synchronization of the different sensors. The camera does not provide any means to synchronize the image capturing with system time. Its clock bias and drift, therefore, had to be estimated in post-processing. The high-grade roll-isolated DMARS-R platform was additionally aboard and served as reference. The performance of the integrated navigation system could thus be well analysed.

At DLR, a dual-frequency GPS and Galileo receiver, the Kodiak GNSS receiver, is currently developed for sounding rockets and micro launch vehicles. It comprises MEMS sensors and interfaces for additional aiding sensors that can be used to compute an integrated navigation solution. A prototype of the Kodiak receiver was additionally on board of the PMWE-1 sounding rocket [3].

The paper is organized as follows: in section 2, the PMWE-1 mission is introduced. In section 3, the used coordinate systems are briefly described. In section 4, the raw IMU measurements are shown and the extraction of the Sun direction vectors out of the camera images is presented. In section 5, the design of the integrated navigation system is illustrated, it is shown how the Sun direction vector measurements are integrated into the navigation error filter, and the navigation performance is analysed without and with GPS and Sun direction vector aiding. The conclusion and outlook is finally given in section 6.

2. PMWE-1 Mission

The PMWE-1 (Polar Mesospheric Winter Echoes) campaign consisted of two differently instrumented sounding rockets that were launched from Andøya Space Center, Norway, in April 2018. Aim of the PMWE campaign was to collect in-situ measurements in the atmospheric layer between 55 and 85 km altitude to better understand observed radar echoes which are most likely produced by neutral air turbulence during winter season [4]. The integrated navigation experiment was accommodated on the second sounding rocket that was launched on 18 April 2018 at 13:00:00 (UTC).

The flight trajectory is shown in Figure 1. The arrows represent the axes of the body-fixed coordinate system. The rocket was not de-spun after motor burnout but kept up spinning even during the coasting flight phase. The azimuth and elevation angles of the sounding rocket's longitudinal axis with respect to North and the horizontal plane, respectively, are illustrated in Figure 2. It can be seen that the rocket keeps the orientation of its longitudinal axis stable in the coasting flight phase between T+60 s and T+240 s. On average, the elevation is about 77 deg above the horizontal plane and about −39 deg with respect to North. The oscillations are due to superimposed precession motion with a period of about 8 s.
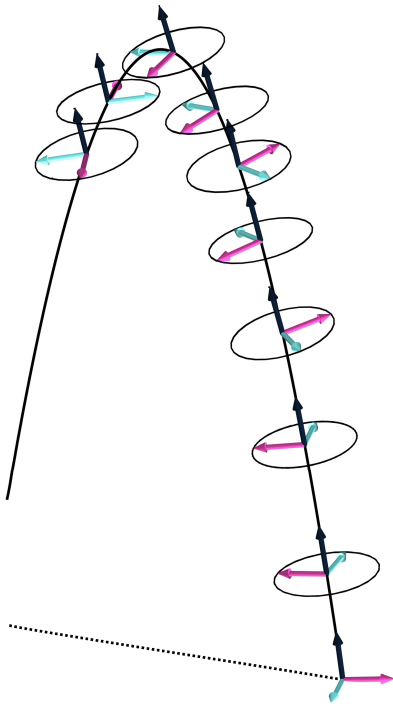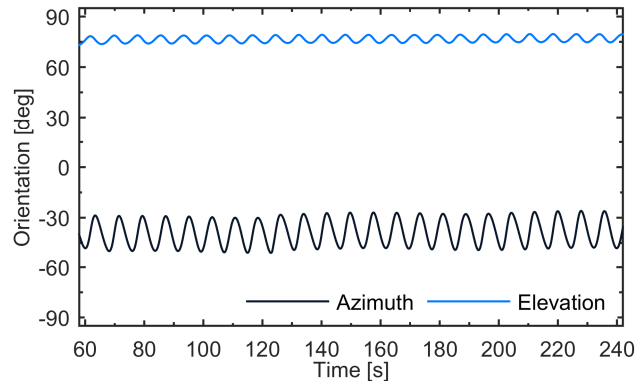
Figure 1: Flight trajectory

Figure 2: Orientation of longitudinal axis
between T+60 s and T+240 s

3. Coordinate Systems

Figure 3 shows the used coordinate systems. The body-fixed coordinate system (b -frame) is located at the reference point of the DMARS-R platform. The z_b -axis is the roll axis and points to the tip of the rocket. The lateral x_b - and y_b -axes are normal to the longitudinal z_b -axis. At the launch pad, y_b points to the launch rail, and x_b completes the orthogonal right hand system. The camera coordinate system (c -frame) is illustrated in Figure 4 and is located at the focal point of the camera. The z_c -axis is aligned with the line of sight of the camera and is parallel to the y_b -axis. The orthogonal x_c - and y_c -axes lie in the image plane of the camera. x_c points to the right and y_c to the bottom of the image. The North-East-Down frame (n -frame) serves as navigation reference frame.
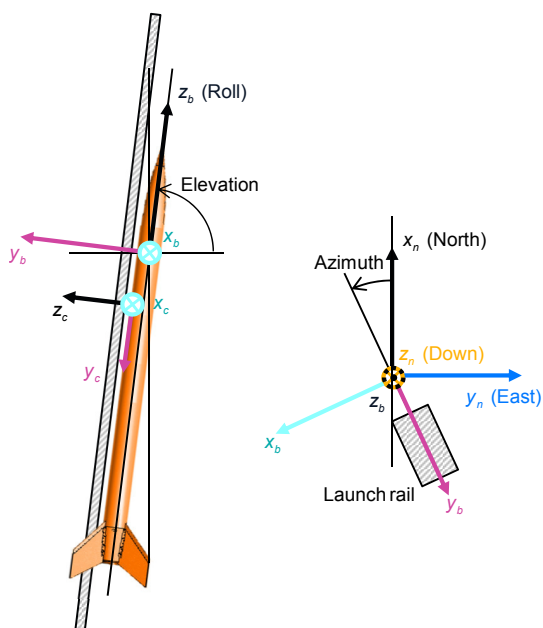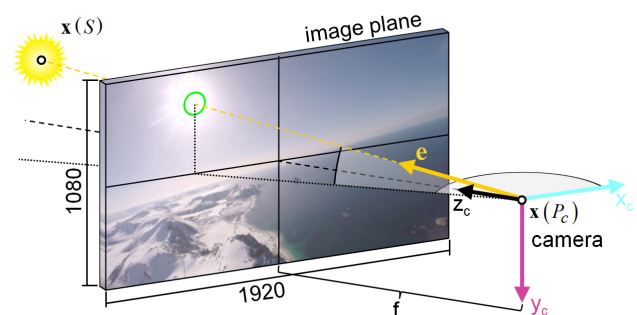

Figure 3: Coordinate systems

Figure 4: Camera coordinate system

Benjamin Braun, Jochen Barf, Markus Markgraf

4. Sensor Measurements

4.1. MEMS IMU Measurements

The STIM300 IMU accommodates three orthogonal gyroscopes and accelerometers. Measurements were sampled with 200 Hz. Figure 5a shows the lateral angular rates and the roll rate that were measured by the gyroscopes in the coasting flight phase between T+60 s and T+240 s. The roll rate is almost constant at 1,283 deg/s. The lateral angular rates oscillate with amplitudes of about 2 deg/s because of the precession motion of the rocket. In Figure 5b, the specific forces that were measured by the accelerometers between T+60 s and T+240 s are plotted. Since the accelerometers were not centrically mounted, the lateral axes experience centrifugal accelerations of –0.65 g in x_b-direction and –0.81 g in y_b-direction. The roll axis measurements are primarily affected by the turn-on bias.

Figure 6 illustrates the Allan standard deviations of the angular rate and acceleration measurements that were recorded during the two hours immediately before lift-off. The dashed lines represent the values that are given in the datasheet for the bias instabilities and the angular/velocity random walk. The determined values are used as parameters for the IMU error models.

In Figure 7, the temperature measured by the x-axis gyroscope is plotted. The temperature is 23 °C at T+60 s and rapidly increases to 47 °C at T+240 s. Due to the large temperature gradient during flight, temperature-dependent effects become noticeable on the IMU measurements and should be considered in the IMU error model.

The performance specification of the STIM300 IMU and the DMARS-R IMU as given in the datasheets and evaluated by the Allan standard deviation analysis are listed in Table 1.
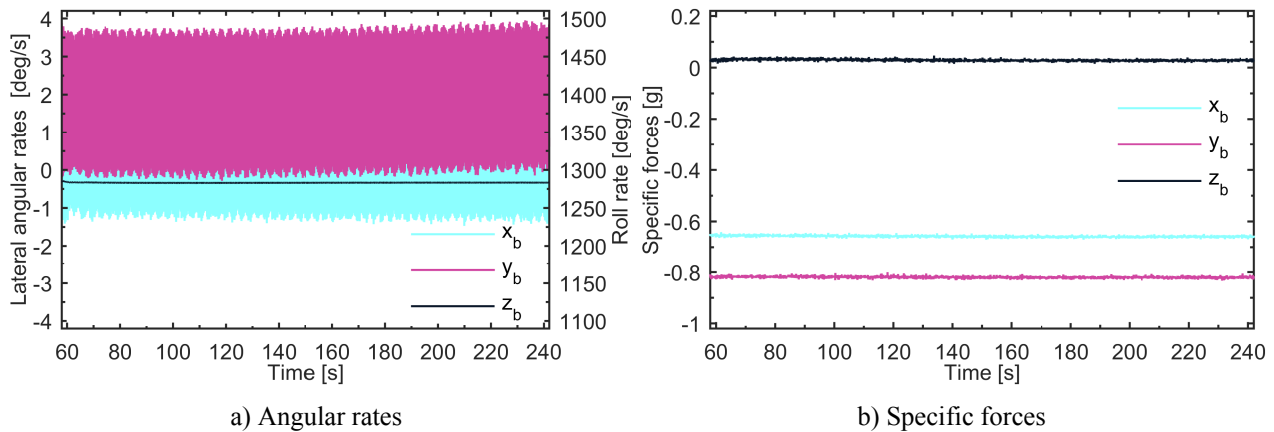

a) Angular rates

b) Specific forces

Figure 5: STIM300 IMU measurements between T+60 s and T+240 s

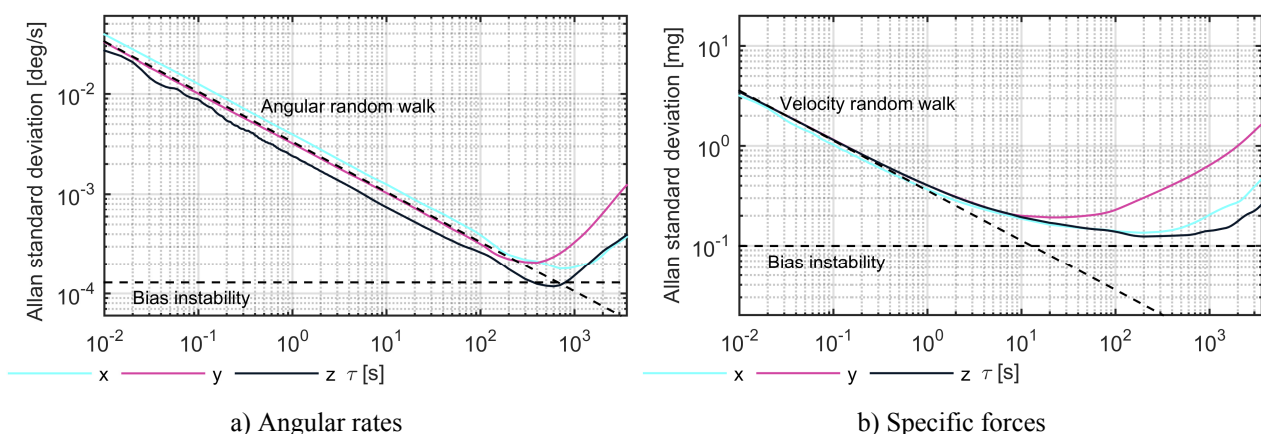a) Angular rates

b) Specific forces

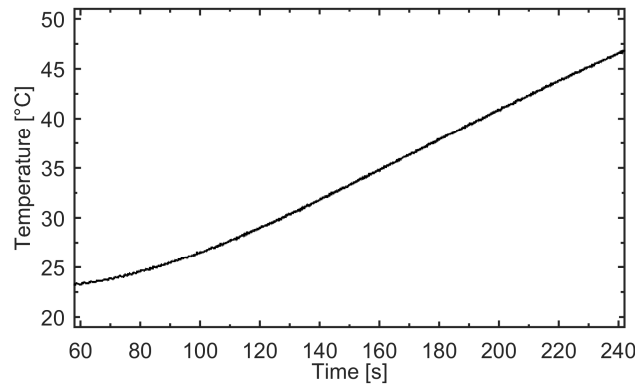Figure 6: Allan standard deviations of the STIM300 IMU measurements shortly before lift-off

4

Figure 7: Temperature of the STIM300 x-axis gyroscope between T+60 s and T+240 s

Table 1: Gyroscope and accelerometer specification

Gyroscope Error			STIM300	DMARS-R	Accelerometer Error			STIM300	DMARS-R
Range	yaw/pitch	deg/s	±2000	±90	Range		g	±30	±10
	roll		±2000	±8000					
Scale factor error		ppm	500	100	Scale factor error		ppm	300	300
Bias repeatability		deg/h	250	0.2	Bias repeatability		mg	0.77	1
Bias instability		deg/h	0.7	n/a	Bias instability		mg	0.15	n/a
actual:	x		0.97	n/a	actual:	x		0.20	n/a
	y		1.12	n/a		y		0.29	n/a
	z		0.64	n/a		z		0.19	n/a
Angular random walk		deg/√h	0.15	n/a	Velocity random walk		m/s/√h	0.21	n/a
actual:	x		0.24	n/a	actual:	x		0.22	n/a
	y		0.19	n/a		y		0.24	n/a
	z		0.14	n/a		z		0.24	n/a
g-dependent	bias	deg/h/g	7	0.2					
	scale factor error	ppm/g	400	n/a					
Bandwidth		Hz	262	50	Bandwidth		Hz	100	300
Axis misalignment		mrad	1	2	Axis misalignment		mrad	1	2

Values taken from datasheets [2,5,6] and Allan variance analysis. Statistical values are 1σ values.

4.2. GPS Measurements

Figure 8 shows the GPS sky plot between lift-off and landing, as seen from the rocket. The labels are at the end of the tracks. The green marked satellites were tracked by the Phoenix GPS receiver. The grey areas mark the pole region where no satellites are expected and the 5 deg receiver elevation mask. Throughout the flight, twelve GPS satellites were tracked by the GPS receiver. Merely at lift-off and at motor burnout, as expected, signal tracking was either completely lost or overshot by several hundred meters for up to ten seconds because of the high jerk, which is usually observed on sounding rockets. Except for these outage periods, the pseudorange and range rate measurements, which were sampled with 5 Hz, are used for aiding the integrated navigation system. Falsified measurements due to the overshooting of the tracking loops at the highly dynamic instants are effectively omitted by an integrity monitor.
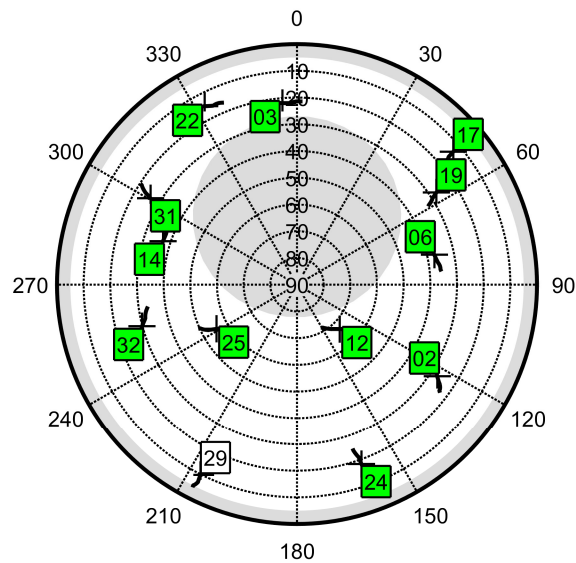
Benjamin Braun, Jochen Barf, Markus Markgraf

Figure 8: GPS sky plot as seen from the rocket between lift-off and landing

4.3. Sun Direction Vector Measurements

The Sun direction vector measurements are derived from the captured images of the GoPro HERO3+ camera. Although this camera is not intended for the use on sounding rockets, it provides surprisingly good pictures. This is mainly due to the high resolution and the fast control of the exposure time, which is required because of the quick changeovers between scenes with dark sky and scenes with bright Sun. The video frame rate was 50 Hz, the image resolution was 1920×1080 (full HD), the horizontal field of view (FOV) was 118.2 deg, and the vertical FOV was 69.5 deg, which corresponds to an equivalent focal length of 17.2 mm. The video was recorded on SD card and could thus only be used in post-processing after recovery of the payload. The camera does not provide means for external time synchronization but runs completely free. The offset and drift of the camera time with respect to the system time had to be estimated afterwards by post-processing. In Figure 9, the mounting of the side-looking GoPro HERO3+ camera in the rocket structure is shown. The objective lens is protected by a thin pane of glass.

The nose cone of the PMWE-1 sounding rocket was thermally protected by an ablative heat shield, which was made of a thin layer of cork that was additionally coated with silicone. Already few seconds after lift-off, the ablating heat shield caused a film of soot on the cover glass of the camera. In hindsight, this was ideal for the function of the camera as Sun sensor since the Sun light was filtered like with a neutral grey filter. Figure 10 shows exemplary camera images taken shortly after lift-off and at T+133 s. The filter effect due to the soot can be clearly seen on the right image.

Figure 9: Side-looking GoPro HERO3+ camera

a) shortly after lift-off (without soot)   b) at T+133 s (with soot)
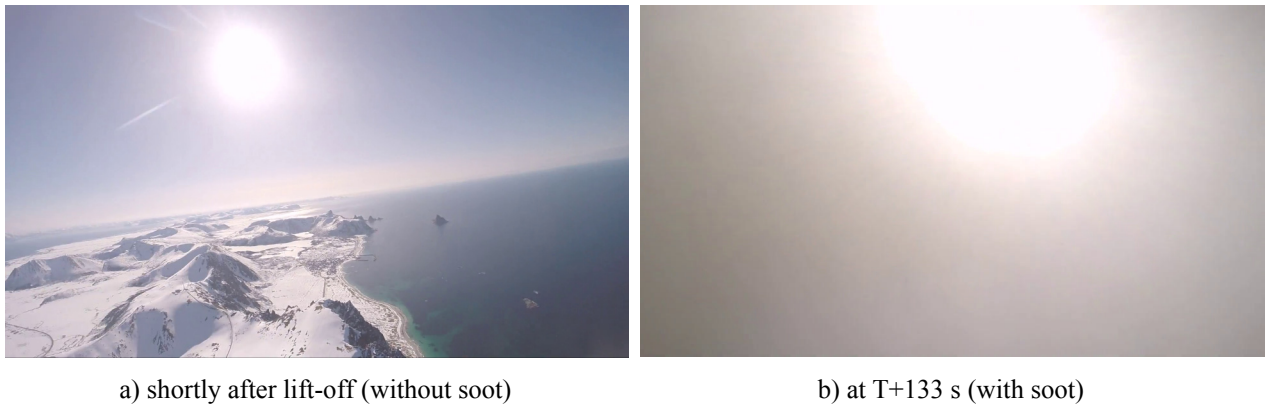
Figure 10: Exemplary camera images

The captured images are processed by an algorithm that had originally been developed to detect the Earth horizon and to subsequently fit a hyperbola to the found curve. The algorithm could be easily adapted to the problem of detecting the Sun in an image. In this case, the algorithm searches for an ellipse that matches the found curve best. In a next step, the coordinates of the midpoint of the ellipse are determined. The single processing steps are illustrated in Figure 11 for the image taken shortly after lift-off. In principal, the image processing algorithm searches all continuous lines along which the brightness gradient exceeds a threshold value. Since the algorithm is intended for Earth horizon detection, only lines that intersect the image border are accounted for in the original version. Since the ellipse of the Sun is a closed curve and does usually not intersect the image border, the image is sectioned into stripes that are less high than the expected image of the Sun as shown in Figure 11a. Now, there is a curve that intersects the borders of the image stripes and the same algorithm can be used. In Figure 11b, the closed curved which is most likely the ellipse of the Sun is extracted. Next, an ellipse is fit to the found curve and the image is undistorted using the intrinsic and extrinsic camera parameters that have been determined before by means of calibration (Figure 11c). Finally, the coordinates of the midpoint of the ellipse are determined (Figure 11d).
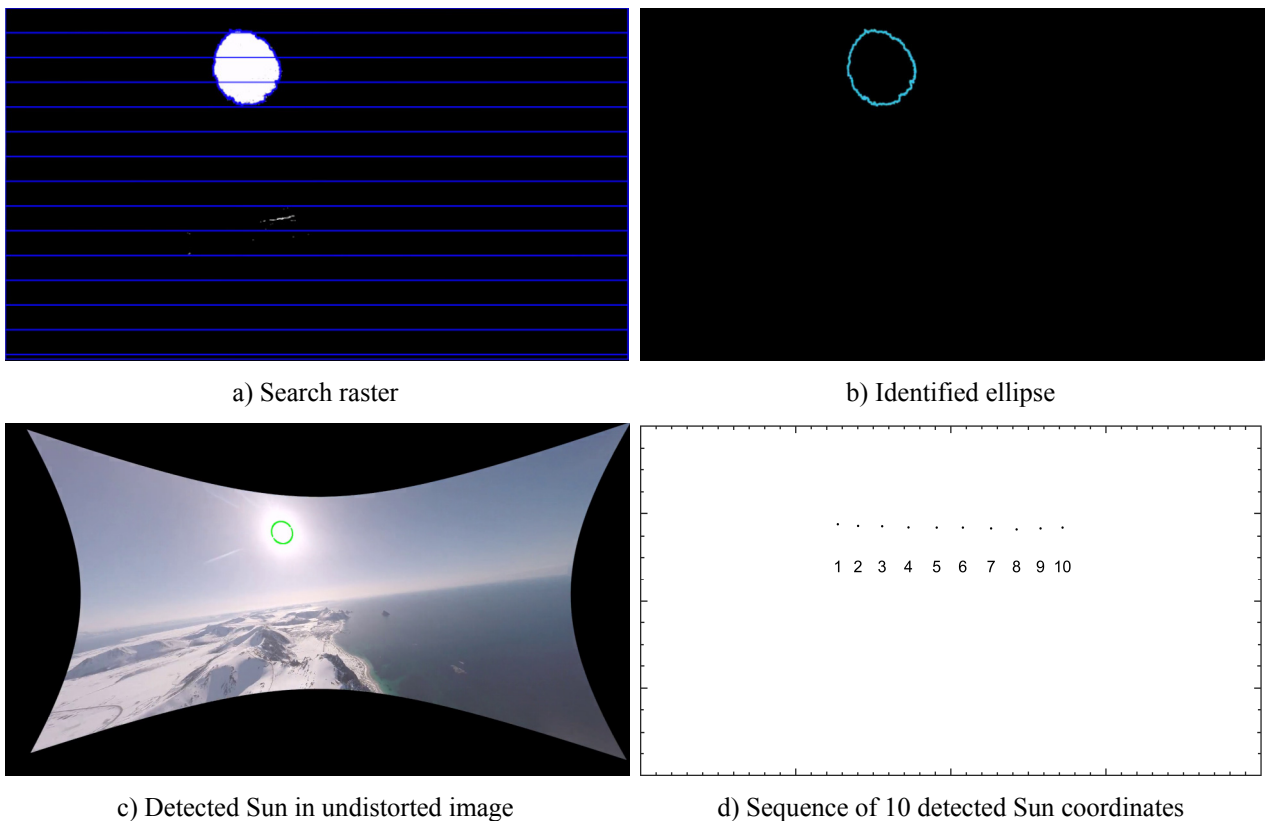
a) Search raster   b) Identified ellipse

c) Detected Sun in undistorted image   d) Sequence of 10 detected Sun coordinates

Figure 11: Image processing sequence shortly after lift-off

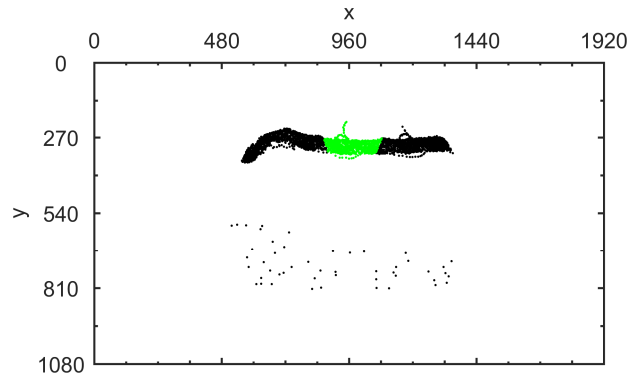Benjamin Braun, Jochen Barf, Markus Markgraf

Figure 12: Image plane with detected Sun midpoints between lift-off and T+240 s. Only the green points near the centre line of the image are used in the integrated navigation filter

Figure 12 shows the image plane of the camera with all Sun midpoints that were detected between lift-off and T+240 s and were flagged as valid by the image processing algorithm. There is obviously a systematic effect because of the crook at the left end of the main trace. The reason for that is mainly the automatic exposure steering of the camera. The rocket rotates counter-clockwise about the longitudinal axis. This means that the Sun enters the image on the left side at every revolution. At this time, the image is strongly overexposed because the camera has increased the exposure time during the dark period immediately before and the Sun appears as big white spot on the image. It takes some milliseconds until the camera reduces the exposure time adequately and the image is not overexposed anymore. Then, the midpoint of the Sun can be determined much more accurately. Therefore, in order to reduce the influence of these systematic errors, only Sun direction vectors in the horizontal centre of the image plane are used in the integrated navigation system. All other points are rejected.

The measured Sun direction vector $\tilde{\mathbf{e}}_c$ is calculated from the image coordinates of the detected Sun X_c and Y_c with

$$\tilde{\mathbf{e}}_c = \begin{pmatrix} X_c/f \\ Y_c/f \\ 1-\sqrt{X_c^2+Y_c^2}\Big/f \end{pmatrix} \tag{1}$$

where f is the focal length of the camera. The vector is normalized to unit length. Figure 13 shows the measured Sun direction vector $\tilde{\mathbf{e}}_c$ that is extracted from the camera images and the Sun direction vector $\hat{\mathbf{e}}_c$ that is expected from the reference orientation solution of the DMARS-R inertial platform. In Figure 14, the difference between the expected and measured Sun direction vectors, $\delta\mathbf{e}_c = \hat{\mathbf{e}}_c - \tilde{\mathbf{e}}_c$, is plotted. It can be seen that there is a good coincidence.

Obviously, the differences of the single vector components feature characteristic correlations with time and bias-like offsets. These non-noise-like offsets are due to the addressed exposure effects, calibration errors of the extrinsic and intrinsic parameters that lead to an erroneous undistortion of the image, camera mounting orientation errors and the clock synchronization error between system and camera time. These errors are accounted for in the navigation error filter by a Sun direction vector error model, which consists of a constant bias with a standard deviation of 0.01, a time correlated error that is represented by a 1st order Gauss-Markov process with a standard deviation of 0.01 and a time constant of 20 s and Gaussian white noise with a standard deviation of 0.01.
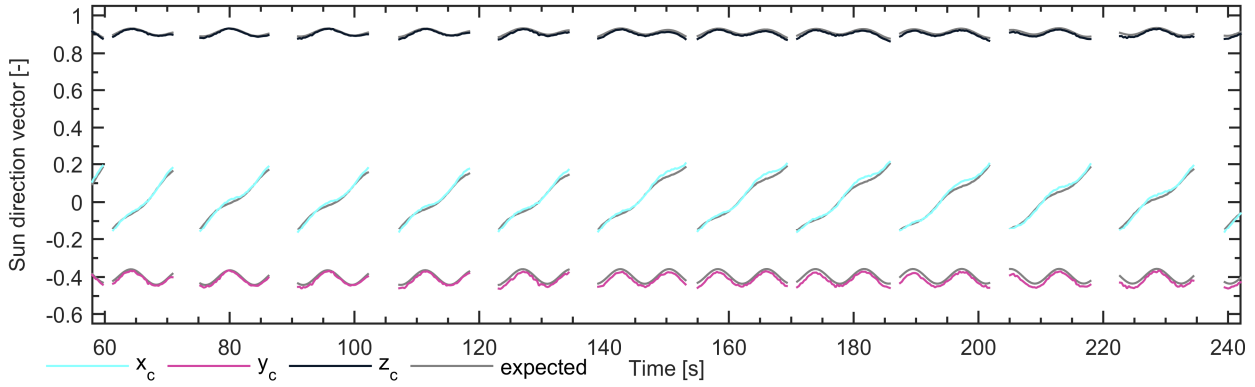
Figure 13: Expected and measured Sun direction vectors in camera coordinate system
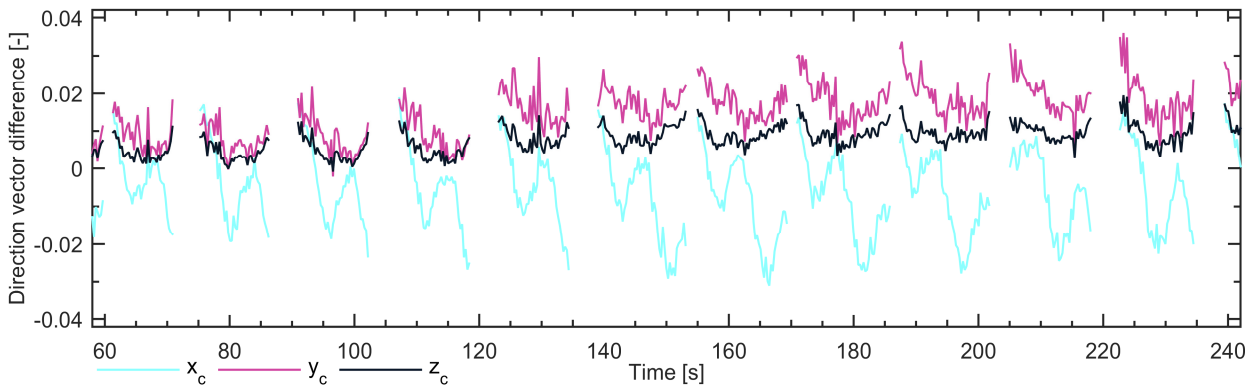

Figure 14: Difference between expected and measured Sun direction vectors in camera coordinate system

5. Integrated Navigation System

5.1. System Design

The design of the integrated navigation system is shown in Figure 15. It corresponds to the well-known design, which is widely used, for example, in unmanned aerial systems to fuse measurements from various navigation sensors and is, for example, described in [7]. The IMU outputs velocity and angle increments which are time-integrated by the inertial navigation system (INS) to obtain the current position, velocity and orientation, beginning from the initial values. By means of a Kalman-filter based navigation error filter, the current position, velocity and orientation errors as well as sensor errors are estimated and used to correct the navigation estimates of the INS and to in-flight calibrate the IMU measurements. The pseudorange and range rate measurements of the GPS receiver and the Sun direction vector measurements of the camera are used to observe the navigation error. The navigation error filter bases upon the navigation error model in ECEF-frame (e-frame)(compare for example [7])

$$\begin{pmatrix} \delta\dot{\mathbf{x}}_e \\ \delta\dot{\mathbf{v}}_e \\ \boldsymbol{\psi}_{e\tilde{e}} \end{pmatrix} = \begin{pmatrix} 0 & \mathbf{I}_3 & 0 \\ \boldsymbol{\Gamma}_e & -2\boldsymbol{\omega}_{ie}\times & -\left(\mathbf{R}_{\tilde{e}b}\tilde{\mathbf{f}}_b\right)\times \\ 0 & 0 & \boldsymbol{\omega}_{ie}\times \end{pmatrix} \begin{pmatrix} \delta\mathbf{x}_e \\ \delta\mathbf{v}_e \\ \boldsymbol{\psi}_{e\tilde{e}} \end{pmatrix} + \begin{pmatrix} 0 & 0 \\ \mathbf{R}_{\tilde{e}b} & 0 \\ 0 & \mathbf{R}_{\tilde{e}b} \end{pmatrix} \begin{pmatrix} \delta\mathbf{f}_b \\ \delta\boldsymbol{\omega}_{ib} \end{pmatrix} \qquad (2)$$

where $\delta\mathbf{x}_e$ is the position error, $\delta\mathbf{v}_e$ is the velocity error, $\boldsymbol{\psi}_{e\tilde{e}}$ is the orientation error, $\mathbf{I}_3$ is the unit matrix, $\mathbf{R}_{\tilde{e}b}$ is the transformation matrix between e-frame and b-frame, $\tilde{\mathbf{f}}_b$ is the acceleration measurement, $\delta\mathbf{f}_b$ is the acceleration error, $\delta\boldsymbol{\omega}_{ib}$ is the angular rate error, $\boldsymbol{\omega}_{ie}$ is the Earth rate, $\boldsymbol{\Gamma}_e$ is the gravity gradient matrix and the $\mathbf{a}\times$ operator forms the skew-symmetric matrix of the vector $\mathbf{a}$. The navigation error model (2) is augmented by models for the IMU errors, pseudorange and range rate errors and Sun direction vector errors. The additional states are either estimated by the navigation error filter or merely statistically considered but not estimated. Table 2 lists all error models and additional error states that are used for this post-processing analysis. Only the linear and g-dependent scale factor errors of the roll axis gyroscope and the turn-on bias of the roll axis accelerometer are estimated, all other errors are statistically considered because their influence on the navigation error is too small or they are noise-like and can thus not be observed by the navigation error filter. The navigation error filter is fine-tuned by adding some extra Gaussian white process noise on the acceleration error and angular rate error inputs.
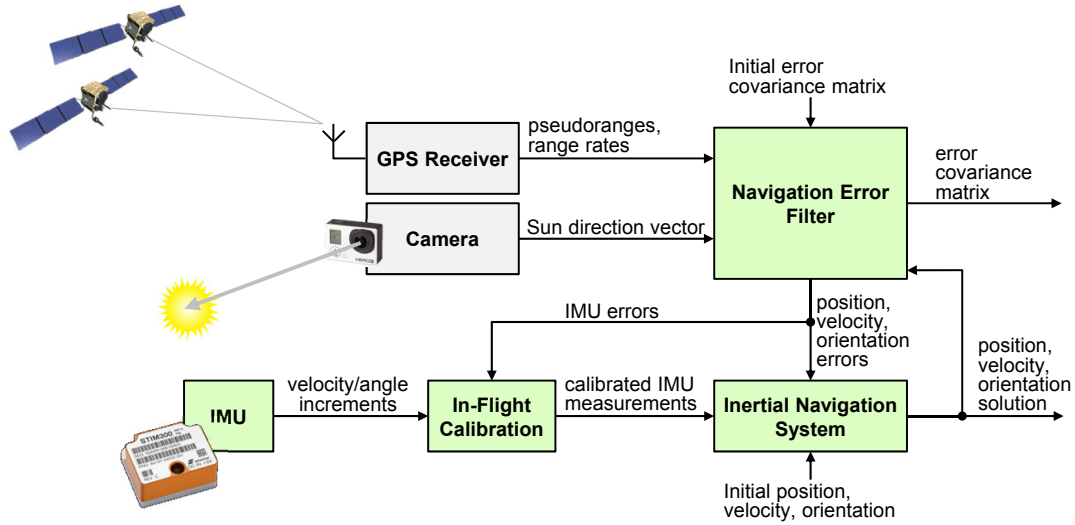
Figure 15: Design of the integrated navigation system

Table 2: Applied error models

Sensor	Error	Model	States	E/C
Gyroscope (per axis)	Turn-on bias	Constant + random walk	1	C
	Scale factor error	Constant	1	C: x,y, E: z
	Angular random walk	White noise	0	C
	Bias instability	Pink noise	5	C
	g-dependent bias error	Constant	3	C
	g-dependent scale factor error	Constant	3	C: x,y, E: z
	Misalignment	Constant	2	C
Accelerometer (per axis)	Turn-on bias	Constant + random walk	1	C: x,y, E: z
	Scale factor error	Constant	1	C
	Velocity random walk	White noise	0	C
	Bias instability	Pink noise	5	C
	Misalignment	Constant	2	C
	Mounting location error	Constant	1	C
GNSS receiver (per channel)	Pseudorange error	White noise + Gauss-Markov	1	C
	Range rate error	White noise + Gauss-Markov	1	C
Sun direction vector	Bias	Constant	3	C
	Short-term noise	White noise	0	C
	Time-correlated noise	Gauss-Markov	3	C

E: estimated, C: considered

5.2. Integration of Sun Direction Vector Measurements into Navigation Error Filter

The navigation error filter uses the difference between the measured Sun direction vector $\tilde{\mathbf{e}}_c$ and the expected Sun direction vector $\hat{\mathbf{e}}_c$, defined in the camera coordinate system c,

$$\mathbf{s} = \tilde{\mathbf{e}}_c - \hat{\mathbf{e}}_c \tag{3}$$

to deduce current navigation state errors and sensor state errors. This is the innovation $\mathbf{s}$ of the Sun direction vector measurement. The expected Sun direction vector $\hat{\mathbf{e}}_c$ is calculated with

$$\hat{\mathbf{e}}_c = \left(\mathbf{R}_{\tilde{e}b} \cdot \mathbf{R}_{bc}\right)^{\mathrm{T}} \frac{\mathbf{X}_e - \hat{\mathbf{x}}_e}{\|\mathbf{X}_e - \hat{\mathbf{x}}_e\|} \tag{4}$$

where $\mathbf{X}_e$ is the position of the Sun, $\hat{\mathbf{x}}_e$ is the current estimate of the position of the rocket, $\mathbf{R}_{bc}$ is the transformation matrix from b-frame to c-frame representing the mounting orientation of the camera, and the

transformation matrix $\mathbf{R}_{\breve{e}b}$ is derived from the current estimate of the orientation of the rocket, for example, given as quaternion $\breve{q}_{\breve{e}b}$, $\mathbf{R}_{\breve{e}b} = \mathbf{R}(\breve{q}_{\breve{e}b})$. The position of the Sun $\mathbf{X}_e$ is calculated according to [8], chapter 6. In order to obtain accurate results, it is necessary to consider the influence of the Moon, Venus, Mars, Jupiter and Saturn.

The Sun direction vector error $\delta\mathbf{e}_c = \mathbf{e}_c - \hat{\mathbf{e}}_c$ is primarily affected by the orientation error $\mathbf{\psi}_{e\breve{e}}$

$$\delta\mathbf{e}_c = \left(\mathbf{R}_{\breve{e}b} \cdot \mathbf{R}_{bc}\right)^{\mathrm{T}} \left(\frac{\mathbf{X}_e - \hat{\mathbf{x}}_e}{\|\mathbf{X}_e - \hat{\mathbf{x}}_e\|} \times\right) \mathbf{\psi}_{e\breve{e}} \tag{5}$$

The influence of the position error $\delta\mathbf{x}_e$ on the Sun direction vector error $\delta\mathbf{e}_c$ is small and is neglected. Furthermore, it is assumed that the calculated position of the Sun $\mathbf{X}_e$ is error-free. Consequently, the observation matrix $\mathbf{H}$ is given with

$$\mathbf{H} = \left(\mathbf{0} \,\middle|\, \mathbf{0} \,\middle|\, \left(\mathbf{R}_{\breve{e}b} \cdot \mathbf{R}_{bc}\right)^{\mathrm{T}} \left(\frac{\mathbf{X}_e - \hat{\mathbf{x}}_e}{\|\mathbf{X}_e - \hat{\mathbf{x}}_e\|} \times\right) \,\middle|\, \cdots\right) \tag{6}$$

The navigation error state vector as defined in (2) is augmented by three states that represent the constant bias and three states that represent the time-correlated error of the Sun direction vector measurements. The innovation covariance matrix $\mathbf{S}$ that is used by the navigation error filter is

$$\mathbf{S} = \mathbf{R} + \mathbf{H}\,\mathbf{P}\,\mathbf{H}^{\mathrm{T}} \tag{7}$$

where $\mathbf{R}$ is the covariance matrix of the Gaussian white noise on the Sun direction vector measurements and $\mathbf{P}$ is the estimated covariance matrix of the augmented navigation and sensor error state vector.

5.3. Inertial Navigation Solution without Aiding

First, the STIM300 IMU measurements are integrated with time by the INS without either GPS or Sun direction vector aiding. The pure inertial navigation solution is compared with the inertial navigation solution of the reference solution of the DMARS-R platform, which is also aided by the GPS measurements. The orientation accuracy of the reference solution is in the range of a tenth degree. The position error between T+60 s and T+240 s, transformed to n-frame, is plotted in Figure 16. The position solution quickly diverges and takes maximum absolute values of 0.52 km in North direction, 0.36 km in East direction and 3.43 km in Down direction. In Figure 17, the difference between the DMARS-R/GPS and STIM300 inertial orientation solutions is illustrated, once transformed to n-frame and once transformed to b-frame. As expected, the roll angle error grows quickly and nearly linearly with time as soon as the spin rate has been built up after a few seconds of flight. After 240 seconds of flight, the roll angle error is already 966 deg, that is about 2.7 revolutions, as can be seen in the n-frame as well as in the b-frame representation. In n-frame, the orientation error oscillates with amplitudes of 14 deg in North direction and 15 deg in East direction with a period of about 88 seconds. In b-frame, the orientation error oscillates with zero mean values about the two lateral x_b- and y_b-axes, which describes the misorientation of the longitudinal axis of the rocket. The orientation errors about the two lateral axes are comparable. Consequently, the unaided position, velocity and orientation solution of the INS with STIM300 IMU input is not adequate for the purpose of navigation.
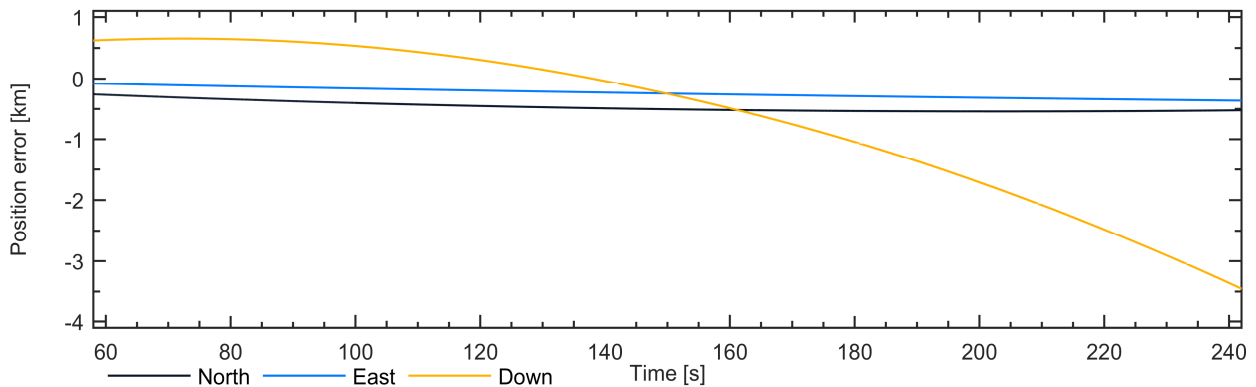

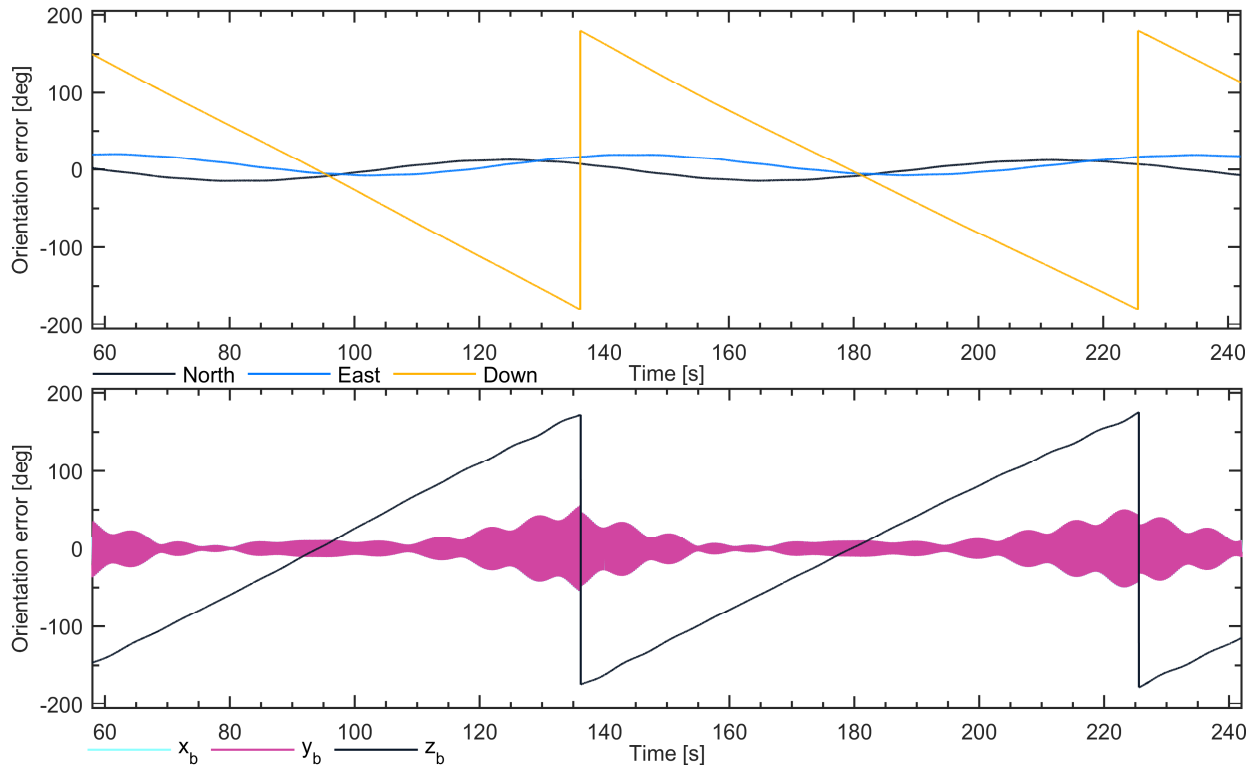Figure 16: Difference between DMARS-R/GPS and STIM300 inertial navigation position solutions

Benjamin Braun, Jochen Barf, Markus Markgraf

Figure 17: Difference between DMARS-R/GPS and STIM300 inertial orientation solutions, transformed to n-frame and b-frame

5.4. Integrated Navigation Solution with Aiding

Now, the INS is aided by the pseudorange and range rate measurements of the GPS receiver and the Sun direction vector measurements. The navigation solution is again compared with the GPS-aided DMARS-R inertial navigation solution. Figure 18 shows the difference between the position solutions of the DMARS-R/GPS and the STIM300/GPS/Sun integrated navigation systems between T+60 s and T+240 s and the combined 3σ standard deviations that are estimated by the DMARS-R/GPS and STIM300/GPS/Sun integrated navigation systems. The position error is primarily controlled by the accuracy of the pseudorange and range rate measurements and the geometry of the GPS satellite constellation. The East position error is slightly smaller than the North and Down position errors because the constellation is more symmetric in eastern direction than in the two other directions as can be seen from the sky plot in Figure 8. The estimated standard deviations are nearly constant and 16.1 m (3σ) in North direction, 14.1 m (3σ) in East direction and 16.8 m (3σ) in Down direction. Figure 19 shows the difference between the orientation solutions of the DMARS-R/GPS and the STIM300/GPS/Sun integrated navigation systems between T+60 s and T+240 s and the estimated 3σ standard deviations. The navigation error filter estimates the orientation error in e-frame, $\psi_{e\tilde{e}}$. For better interpretability, it is transformed once to n-frame, $\psi_{n\tilde{n}}$, and once transformed to b-frame, $\psi_{b\tilde{b}}$. In n-frame, the maximum values of the actual orientation error are 1.35 deg in North direction at T+226 s, 1.20 deg in East direction at T+126 s and 2.36 deg in Down direction at T+239 s. Transformed to b-frame, the orientation errors about the two lateral x_b- and y_b-axes oscillate, their mean values, however, are zero. The two lateral orientation errors are more or less equal as in the unaided case. The maximum amplitude is 1.49 deg at T+226 s. The estimated 3σ standard deviations depict the actual errors well. The orientation error about the roll axis, z_b, does not oscillate but features a trend. Its maximum absolute value is 2.13 deg at T+240 s. The regular peaks of the roll orientation error standard deviation are due to the fact that the Sun is periodically not visible in the camera image. In these periods, the orientation error about the roll axis quickly grows because of the roll axis gyroscope scale factor error. Obviously, the estimated standard deviation does not perfectly describe the actual roll angle error. This deficiency most likely stems from the insufficient time synchronization of the system clock and the camera clock. Furthermore, the systematic Sun direction vector error seems to be not yet fully understood and correctly modelled. Figure 20 shows the three components of the innovation vector $\mathbf{s}$ and the corresponding 3σ standard deviations of the innovation covariance matrix $\mathbf{S}$. It can be seen that the actual innovation curves lie well within the estimated 3σ boundaries. Consequently, with the given setup, an orientation accuracy of better than 2.6 deg (3σ) could be achieved on the PMWE-1 sounding rocket.
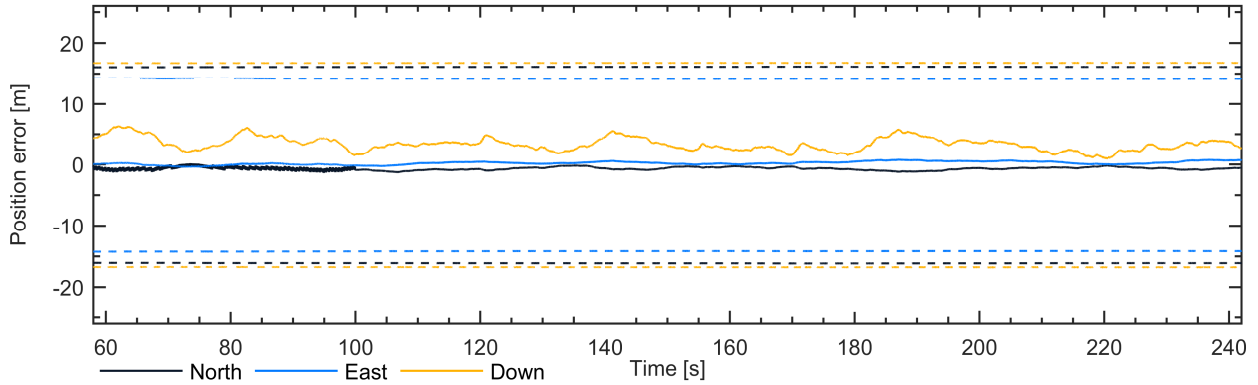
Figure 18: Difference between DMARS-R/GPS and STIM300/GPS/Sun position solution and estimated 3σ standard deviations
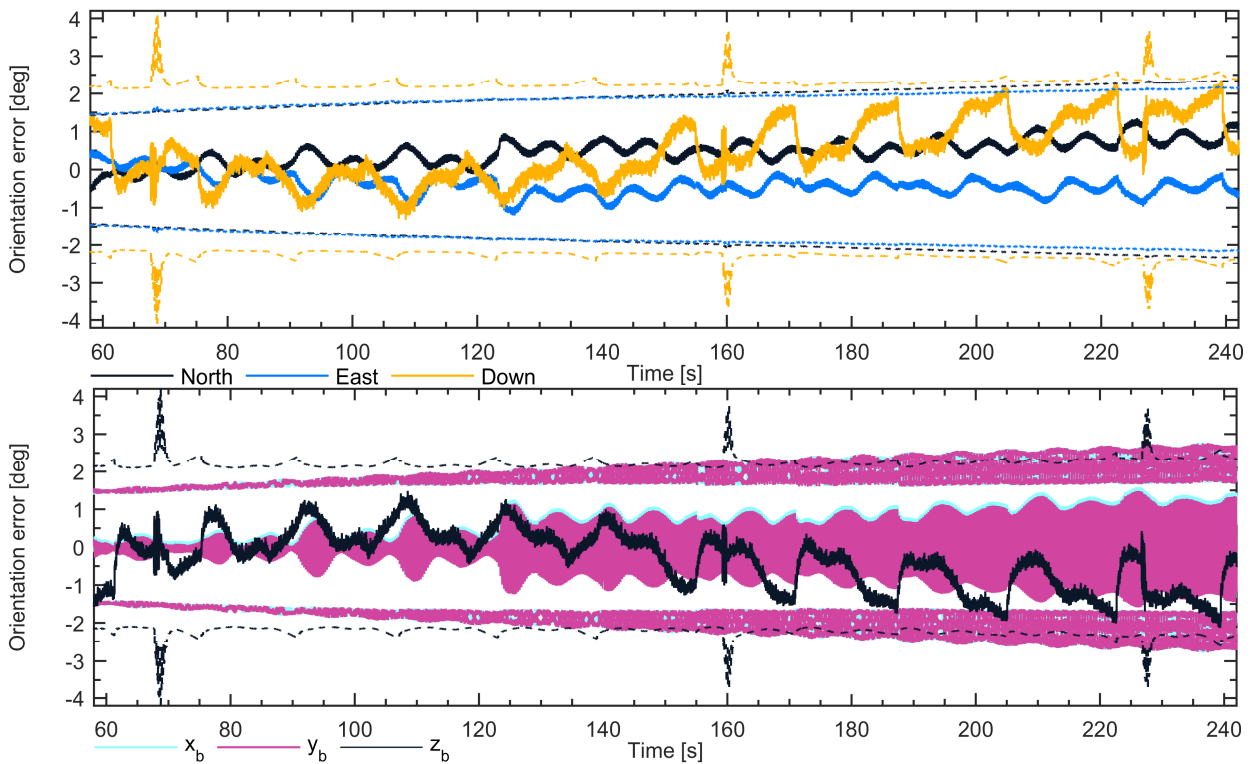

Figure 19: Difference between DMARS-R/GPS and STIM300/GPS/Sun orientation solutions and estimated 3σ standard deviations, transformed to n-frame and transformed to b-frame
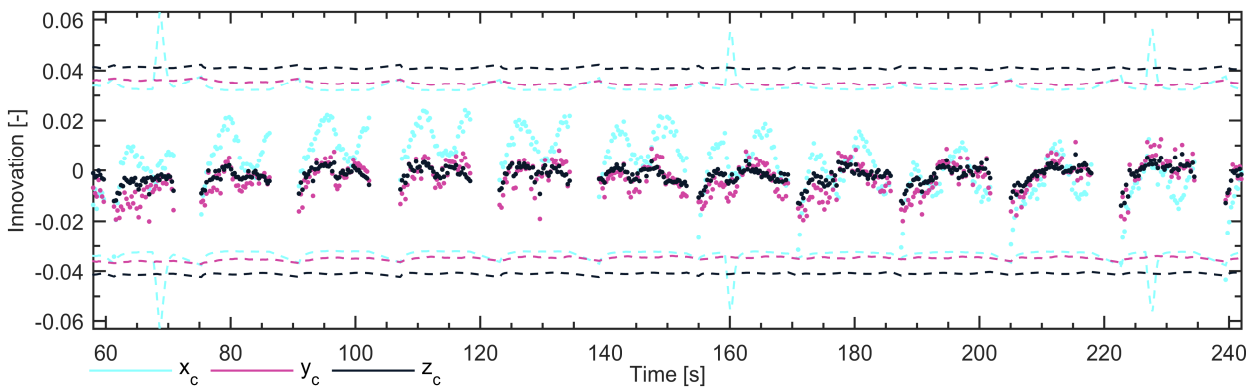

Figure 20: Innovation of the Sun direction vector measurements

6. Conclusion and Outlook

The post-processing study yielded promising results concerning the estimation of the position, velocity and orientation of highly dynamic spin-stabilized sounding rockets by means of a tactical-grade MEMS IMU. If the INS is unaided, the orientation error quickly grows especially about the roll axis due to the scale factor error of the roll axis gyroscope and transforms to the two other axes in turn. Subsequently, the position error quickly increases such that an unaided INS that uses a MEMS IMU is not suitable for spin-stabilized sounding rockets. If the INS, however, is aided by the pseudorange and range rate measurements of a GPS receiver and Sun direction vector measurements that are extracted from camera images, it has been illustrated that it was possible to obtain orientation accuracies of better than 0.87 deg (1σ) or 2.6 deg (3σ), respectively, on the flight of the PMWE-1 sounding rocket. The accuracy of the position and velocity solution is mainly driven by the quality of the GPS measurements.

The presented integrated navigation system comprising robust and lower-cost components may, therefore, be a veritable alternative to a sensitive roll-isolated inertial navigation platform if the achievable navigation solution accuracy, which is roughly one order of magnitude lower, fulfils the requirements of the flight experiment. The integrated navigation solution may serve as backup for flight tracking and range safety in case of GNSS outages.

The orientation solution that has been obtained in this post-processing study is affected by errors due to the inaccurate mounting of the camera and the missing time synchronization of the camera time with the system time. The achievable accuracy may thus be even better if the GoPro HERO3+ camera is replaced by a more robust camera that allows external image capturing and time synchronization and that can be deterministically mounted into the rocket structure. Next, a real-time capable system shall be developed which is able to provide position and velocity estimates to flight guidance and range safety even during short GNSS outages. The automatic exposure steering of the GoPro cameras is excellent. It has been seen that the steering has to be very fast. However, it has to be analysed if a constant exposure time that is adapted to the view into the Sun yields better results. Furthermore, different optical filters shall be tested that display the Sun on the image more sharply and thus simplify Sun detection. The system will be again tested on the next PMWE campaign. Then, the heat shield will be improved such that the lens will not be soiled by the soot of the ablating heat shield. It is intended to additionally detect the Earth horizon on the camera images and to use the extracted Earth centre direction vector for aiding the integrated navigation system. Finally, it is thought about measuring the Sun direction vector by means of dedicated Sun sensors.

Acknowledgement

References

[1]   Beader, M. E. 2000. Application of Roll-Isolated Inertial Measurement Units to the Instrumentation of Spinning Vehicles. Sandia Report SAND2000-3070, Sandia National Laboratories.
[2]   Inertial Science. 1999. Digital Miniature Attitude Reference System DMARS-R. Datasheet.
[3]   Grillenberger, A., Braun, B., and Markgraf, M. 2019. The Kodiak GNSS Receiver for Microlaunchers and Sounding Rockets. In: *Proceedings of the 42nd AAS Annual Guidance and Control Conference*.
[4]   Strelnikov, B., Rapp, M., Strelnikova, I., Chau, J. L., Latteck, R., Luebken, F.-J., Friedrich, M., Asmus, H., Renkwitz, T., and Staszak, T. 2018. PMWE-1 sounding rocket campaign. In: *42nd COSPAR Scientific Assembly*.
[5]   Sensonor. 2018. STIM300 Inertia Measurement Unit. Datasheet, TS1524 rev. 24.
[6]   Sensonor. 2015. Datasheet Addendum: STIM300 other gyro ranges. TS1625 rev. 1.
[7]   Groves, P. D. 2013. Principles of GNSS, Inertial, and Multisensor Integrated Navigation Systems. 2nd ed., Artech House, Boston.
[8]   Montenbruck, O., and Pfleger, T. 2000. Astronomy on the Personal Computer. 4th ed., Springer, Heidelberg.